Additive Manufacturing 51 (2022) 102626

Contents lists available at ScienceDirect

Additive Manufacturing

journal homepage: www.elsevier.com/locate/addma

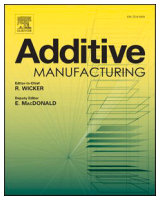

Predicting build density in L-PBF through in-situ analysis of surface topography using powder bed scanner technology

Qingyang Lu [a], Marco Grasso [b], Tan-Phuc Le [a,c], Matteo Seita [a,c,d,*]

[a] School of Mechanical and Aerospace Engineering, Nanyang Technological University, Singapore 639798, Singapore
[b] Department of Mechanical Engineering, Politecnico di Milano, Via La Masa 1, 20156 Milano, Italy
[c] Singapore Centre for 3D Printing, School of Mechanical and Aerospace Engineering, Nanyang Technological University, Singapore 639798, Singapore
[d] School of Materials Science and Engineering, Nanyang Technological University, Singapore 639798, Singapore

ARTICLE INFO

Keywords:
In-situ monitoring
Machine vision
Powder bed image
Porosity
Density
Superpixel

ABSTRACT

The layerwise nature of additive manufacturing (AM) allows for in-situ monitoring of the consolidate material to identify defects on the fly and produce parts with improved reliability and performance. The main challenge in this paradigm, however, is that current methods have either limited measurement throughput or produce signals that are difficult to interpret and to relate to build properties. In this work, we present a new methodology that combines high-throughput in-situ measurements during laser powder bed fusion (L-PBF) with robust and unbiased numerical image analysis to predict build density from the surface topography of the consolidated material. The method relies on high resolution and large field of view optical scans of the layer—acquired through our powder bed scanner (PBS) technology—which we segment into "superpixels" to capture local and distributed differences in surface morphology and roughness. The high accuracy of our predictions together with the fast data acquisition and analysis enabled by the PBS and the low-dimensionality of the optical dataset after segmentation make our methodology an ideal candidate for in-line monitoring of materials produced by L-PBF. In addition, the ability to indirectly deduce a specific material property—namely density—as opposed to inferring a qualitative descriptor related to it makes our methodology unique and transferable to commercial powder bed fusion processes.

1. Introduction

The layer-wise material forming process typical of additive manufacturing (AM) technology offers unique opportunities to assess build quality layer by layer throughout the entire volume of parts produced. In theory, this capability may enable defects identification both at the material level [1] as well as at the part geometry level [2], which could either be directly rectified during the manufacturing process or leveraged to inform the performance and lifetime of parts more accurately. In practice, however, this paradigm relies on the ability to interpret the data acquired at each layer using different in-situ and in-line measurements [3].

A wealth of sensing methods and data processing algorithms have been proposed to capture different signatures of the physical phenomena involved during metal AM processes and infer the presence of anomalies or defects in the build. An overview of the wide and rapidly growing literature on this topic can be found in recent review studies by McCann et al. [2] and Grasso et al. [4]. Among the different in-situ monitoring strategies developed for laser powder bed fusion (L-PBF) processes, many rely on layerwise measurement of the topography of consolidated layers to detect anomalies and estimate part quality. Table 1 reports some relevant works in this field, classified according to sensing method, spatial resolution, and field-of-view (FOV).

As shown in Table 1, the mainstream research in this field relies on using one or more cameras—typically mounted off-axis with respect to the laser energy source—to capture images of the consolidated layers through viewports available at the front or on the top of the machine chamber. Depending on the number of cameras and on their arrangement, the topographic information acquired may be two- or three-dimensional (3D). Employing lighting sources typically yields two-dimensional (2D) images of the surface layer, whose pixel intensity variation may be analyzed to identify irregular patterns on the solid metal surface or powder bed recoating errors. Fringe projection—which makes use of optical cameras (usually in a stereo-vision configuration)

* Corresponding author at: School of Mechanical and Aerospace Engineering, Nanyang Technological University, Singapore 639798, Singapore.
E-mail address: mseita@ntu.edu.sg (M. Seita).

https://doi.org/10.1016/j.addma.2022.102626
Received 23 October 2021; Received in revised form 14 January 2022; Accepted 14 January 2022
Available online 17 January 2022

and projectors—provides 3D information on the layer topography. This approach allows quantifying the size and morphology of different features, such as deposited spatter particles, layer roughness, and surface profiles of the consolidated metal layer. Another important aspect that emerges from Table 1 is the trade-off between spatial resolution and FOV in layerwise monitoring of the L-PBF process. On the one hand, large-area inspection of layers restricts the maximum spatial resolution of images to ~20 μm or ~30 μm [6,7,10]. On the other hand, using techniques with higher spatial resolution limits the maximum area that can be imaged to typically less than 100 mm × 100 mm, which may not be representative of the entire layer [5,21,22].

To overcome the spatial resolution-FOV trade-off and provide detailed information across the entire area of the layer, our team recently proposed an in-line monitoring method based on the powder bed scanner (PBS) technology [23]. The PBS relies on a line-scan imaging sensor—the very same sensor found in flatbed document scanners—which is directly mounted onto the recoater arm [23]. This set-up allows using the recoating device to capture high resolution (~5 μm/pixel) images at 4800 dots-per-inch (DPI) over an area of 210 × 297 mm^2 at a speed that is comparable with typical recoating velocities [24]. At that spatial resolution, individual powder particles are clearly visible. Moreover, the PBS technology provides 3D topographic information of the layer owing to the narrow depth of field of the line-scan sensor. By correlating the local level of focus in the image with the line-sensor distance from the layer, it is in fact possible to quantify the height or depth of features on the powder bed. Barrett et al. [26] proposed a similar approach by blade-mounting a laser triangulation line-scan system to reconstruct the height-map of the powder bed. Although their monitoring system allows the detection of lack-of-fusion defects and deposited spatters in addition to the height-maps, it is limited by the trade-off between FOV and spatial resolution.

While all the above-mentioned methods provide some level of anomaly detection capability during L-PBF—either on re-coated powder layers or on consolidated layers—there is a need to link this information to the presence of actual defects in fabricated parts to predict build quality. It is also essential to develop in-line data processing methods that enable on-the-fly data analysis and efficient data storage while preserving the ability to extract and model the actual information. The specific problem we address in this study consists of inferring build density from in-situ analysis of the surface patterns in the consolidated material, layer by layer. Such a capability may open novel industrial uses of powder bed imaging methods in L-PBF. Indeed, it would allow time- and cost-effective detection of surface anomalies which have been ascribed to poor build quality and would help reduce the experimental efforts devoted to materials development and process optimization. Within this framework, our proposed approach involves two major innovations in the field of in-line monitoring during AM processes. The first regards the layerwise image processing methodology, which relies on the segmentation of the raw data (acquired by means of the PBS technology on individual layers) into so-called "superpixels". This approach enables capturing region-level differences in surface morphology, roughness, and intensity of reflected light in a more computationally efficient and a more holistic way compared to the pixel-wise analysis of the images. The second innovation regards how we predict part quality from the in-situ optical measurements. Rather than training a classifier to estimate part quality indirectly following predefined categories—as it was done in several previous studies [5,6,15,16,27]—we predict build density. We confirm our predictions using X-ray computed tomography (CT) measurements and benchmark the higher performance of our method against others. Although the proposed methodology relies entirely on the PBS technology, we believe it could be extended to other in-line monitoring techniques which employ different machine vision equipment.

2. Proposed methodology

Our approach relies on processing the PBS micrographs using a superpixel-segmentation algorithm to highlight surface patterns in solidified layers and lighten the image processing time. Superpixels divide an image into structurally meaningful groups of pixels, whose morphology naturally adapts to gradients and borders within the image [28]. Since superpixels carry information on region-level properties—including the shape of the pixel group, topology, intensity and contrast variations, and blurriness—and since the number of superpixels is lower than that of pixels in the raw image, the segmentation provides a more holistic information and yields a lighter dataset compared to original micrographs. In this work, we focus on the monitoring of the L-PBF process through the analysis of the surface topography of consolidated layers of stainless steel 316 L (SS316L) and define two key superpixel attributes to predict build density. The methodology—which can be fully integrated within L-PBF processes—consists of three main steps:

Table 1
Summary of literature devoted to in-situ layerwise monitoring in L-PBF.

Sensing method	Illumination	Lateral resolution (μm/pixel)	Vertical resolution (μm/pixel)	Field of view (mm)	References
Off-axis imaging in visible range	Direct or diffuse	7	Not applicable	~15 × 28	Aminzadeh and Kurfess [5]
		10 – 13		40 × 60	Lu et al. [6]
		20		50 × 50	Caltanissetta et al. [7]
		24			Kleszczynski et al. [8], zur Jacobsmulhen et al. [9]
		20 – 30		40 – 105 × 40 – 105	zur Jacobsmulhen et al.[10]
		15 – 50		Not specified	Foster et al. [11]
		50			Gobert et al. [12]
		45 – 88			Abdelrahman et al.[13]
		125			Pagani et al. [14]
		20 – 290			Scime et al. [15]
		290			Scime and Beuth [16]
	Fringe projection	6.8	Not specified	28 × 15	Land et al. [17], Zhang et al. [18]
		72 – 76		Not specified	Dickins et al. [19]
		100	< 10		Kalms et al. [20]
Inline coherent imaging	Laser beam exposure	30	7	Not specified	Fleming et al. [21]
		100	25	44 × 44	DePond et al. [22]
Blade-mounted sensor	Embedded in the transducer	5.3	< 50	210 × 297	Le and Seita [23], Le et al. [24]
		5.97	Not applicable	98 (width)	Fischer et al. [25]
	Laser	20	Not specified	Not specified	Barrett et al. [26]

1) PBS image acquisition of consolidated layer right after laser scanning and before re-coating of a new powder layer,
2) Superpixel segmentation of the PBS micrographs following a simple linear iterative clustering (SLIC) algorithm [29,30],
3) Evaluation of the intensity and focus level variations within each superpixel and their surroundings, which we identify as the two most relevant attributes to predict build quality.

2.1. Powder bed image acquisition and SLIC segmentation

The first step in the methodology is to acquire one micrograph for each consolidated layer (i.e., after laser scanning) using the PBS technology [23]. That requires two calibration stages: (i) synchronizing the recoater speed with that of the sensor data acquisition rate to obtain distortion-free images; and (ii) aligning the PBS sensor such that its imaging plane coincides with the powder layer to obtain focused images. The first calibration is taken care of automatically by the signal processing controller, as detailed in our previous publication introducing the PBS technology [23]. Aligning the position of the sensor to ensure focused image acquisition, on the other hand, is carried out by the operator before each L-PBF experiment. This second calibration consists of setting the sensor working distance from the powder layer equal to its focal distance, which is ~3 mm (as detailed in the aforementioned publication). First, we raise the substrate (which we use as a reference plane) above the nominal laser focusing plane by $(3 + t/10^3)$ mm, where t is the powder layer thickness in μm. This distance equals the sensor working distance plus one powder layer thickness (of t μm). We then lay the sensor down on the substrate before fixing it to the recoater arm. Subsequently, we lower the substrate down by 3 mm, lay the recoater blade on it and fix the blade to the recoater arm. Finally, we lower the substrate by t μm to set the correct powder layer thickness. As a result, the distance between the PBS sensor and the recoater blade tip (and thus, the powder layer surface) is constant and maintained at 3 mm. At the end of the calibration, we can acquire undistorted and focused images of the entire build area.

It is noteworthy that we convert the micrographs into grayscale images because the color information does not contribute significantly to the characterization of surface patterns. Nevertheless, the methodology is easily extendable to colored scans. Moreover, we apply no filters to remove shadowing in the scans, which stem from surface asperities. In fact, shadows carry information about the specimen's surface roughness (which we use to estimate build density). Indeed, shadows are rare across specimens with relatively smooth surface. By contrast, they become more ubiquitous when imaging specimens with higher surface roughness, giving rise to scans with larger intensity variations. These features are the result of melting or solidification instabilities, which we speculate (and demonstrate in this work) are the precursor of defects and thus lead to low density builds.

The second step employs a SLIC-based superpixel segmentation of the raw micrographs. The SLIC algorithm is based on a clustering operation that groups pixels together based on intensity, similarity, and proximity in the image. The resulting groups are the superpixels. The clustering operates in a 3D parametric space, where the first parameter corresponds to the pixel intensity, I, and the other two represent the x and y pixel coordinates in the image. The algorithm starts by setting initial superpixel clusters of equal size on a regular grid with P centers, $C_k = [I_k, x_k, y_k]^T$, where $k = 1,\ldots,P$, and P is the user-defined number of superpixels that the segmented micrographs must have. The cluster centers are then moved in an $n \times n$ neighborhood (where usually $n = 3$) and placed in the lowest gradient position of intensity within the neighborhood [30]. After this superpixel center perturbation, each pixel in the image is linked to the nearest cluster center within a search area of size $2S \times 2S$, where S is the superpixel size parameter defined as $S = \sqrt{\frac{M \times N}{P}}$ and $M \times N$ is the raw image size. To determine the nearest cluster center, we use the following distance metric, D_s, between the i-th pixel and the k-th superpixel center,

$$D_s = \sqrt{{d_{gray}}^2 + \left(\frac{m}{S} d_{xy}\right)^2}. \quad (1)$$

Here, d_{xy} is the Euclidean distance between the i-th pixel and the k-th superpixel center and d_{gray} is the Euclidean distance of their intensities, defined as $d_{gray} = \sqrt{(I_k - I_i)^2}$. The SLIC algorithm ensures that the superpixel size, S, is approximately equal to ensure high computational efficiency. The number of superpixels as input of the SLIC algorithm can be imposed by setting S equal to a characteristic dimension of the surface pattern. The choice of S depends on both the spatial resolution of the input image and the minimum size of the surface features of interest. S increases with the area of consolidated material on the layer for a constant value of P. A superpixel shall consist of a high number of pixels to enable an effective dimensionality reduction but, at the same time, its size shall be small enough to assess surface information at high spatial resolution. It is worth noting that P—whose value is user-defined—dictates the superpixel size, S. Thus, we recommend choosing P to ensure an appropriate value of S. Section 4 reports a discussion on how to estimate S.

The parameter m in Eq. (1) controls the compactness of a superpixel. The greater the value of m, the more regularly shaped superpixels are (i.e., more towards the shape of a square or a circle). By contrast, the smaller the value of m, the more superpixels will adhere to region boundaries in the image, yielding more irregularly shaped superpixels. m is iterated to optimize the trade-off between the shape of the superpixel and how well it adheres to boundaries in the image [30,31]. Pixels are assigned to superpixels until a stop condition on the residual error, E, is met. Additional details about the SLIC algorithm together with a discussion on the influence of intrinsic parameters like neighborhood size n and the stop condition can be found in [29,30].

We selectively run the SLIC algorithm on portions of the micrographs—or regions of interest (ROI)—which contain solid material (i.e., regions of the powder layer which have been consolidated by the laser). This information is typically available from the CAD file of the object to be produced by L-PBF, which indicates the nominal shape of the part in each layer. Using this information as a "mask" and applying it to the raw scans reduces the size of the raw images and speeds up image analysis. Fig. 1(a) shows an example of a digitally magnified micrograph of the solidified layer of a cylindrical specimen. Fig. 1(b) and 1 (c) show an example a PBS-acquired micrograph with a mask applied to isolate the ROI and the resulting segmentation into the P_j superpixels, where $j = 1, \ldots, J$, J being the total number of layers.

2.2. Superpixels attributes

The third step of the methodology involves the analysis and computation of two superpixel attributes across all layers—namely intensity and focus level variation across all pixels within a superpixel—as a proxy of topographical properties of the metal surface. We select these two attributes based on the intuition that deviations from a flat and homogenous surface produce intensity variations due to shadowing and to differences in local focus level because surface protrusions or depressions fall out of the focal plane of the line-scan sensor [23].

By construction, superpixels include pixels with similar intensity. We employ a histogram-based analysis to compute the intensity variation both within each superpixel as well as within adjacent superpixels. To this end, we compute an adjacency matrix of superpixels within the same ROI on the layer to automatically identify and label neighboring superpixels. The adjacency matrix carries the following information:

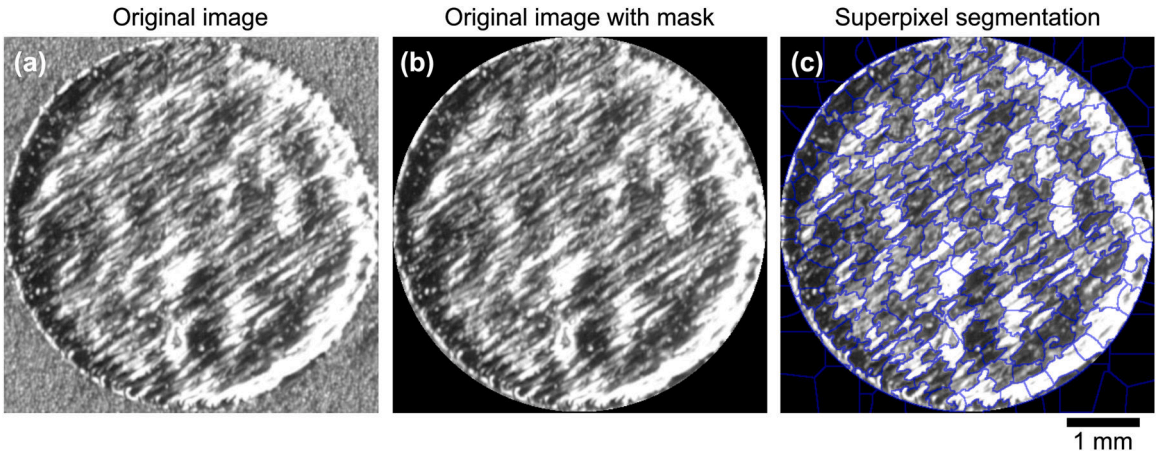

Fig. 1. (a) Example of a PBS-acquired micrograph of a solidified layer; (b) PBS-acquired micrograph after masking with nominal shape (mask) of the consolidated metal (here SS316L); and (c) resulting SLIC-based superpixel segmentation.

1) The adjacency between each superpixel and itself is 0 (all elements along the diagonal of the matrix are 0),
2) The adjacency between two superpixels is 1 if they have at least one pixel edge in common (adjacency of order 1),
3) The adjacency between two superpixels is 2 if there is at least one superpixel that has adjacency of order 1 with both of them (adjacency of order 2), etc.

A graphical representation of superpixels of adjacency order 1 and 2 with respect to a given superpixel is shown in Fig. 2.

The analysis of the histograms of groups of superpixels with adjacency order up to $q = 2$ across each solidified layer is computationally demanding as we capture high resolution micrographs of the entire powder bed. To process high-resolution images in a computationally efficient way we use principal component analysis (PCA) and project the multidimensional histograms into a lower dimensional space. If the PCA is successful, the first few principal components (PCs) [32–34]—which consist of linear combinations of original variables—should capture the largest portion of data variability; namely the most salient information about the surface pattern of the solidified layer. We discuss the main steps of this algorithm in the following.

Based on the adjacency matrix, we compute a histogram of intensities within a group of superpixels with adjacency order up to $q = 2$. This histogram is associated to the k-th superpixel that is in the center of the group. Thus, each superpixel has its own histogram. There will be a total of P_j histograms for each j-th solidified layer, which are used as input to form a histogram data matrix, $\mathbf{X}$, as illustrated in Fig. 3. Each histogram can be treated as a B-variate vector, where B is the number of bins. Let $\mathbf{X}$ be a data matrix in which each row corresponds to the histogram of a group of superpixels with adjacency order up to q. Such a histogram contains information on pixel intensities within the superpixel itself as well as within neighbouring superpixels with adjacency order up to q. If $\mathbf{X}$ includes all histograms computed in the j-th solidified layer, then $\mathbf{X}$ is a $P_j \times B$ matrix. We then carry out PCA on $\mathbf{X}$ to compute a linear combination of frequency values in different bins that maximizes the explained variability (i.e., the first PC). The weights of such a linear combination—referred to as "loadings"—are the elements of the first eigenvector of $\mathbf{X}$; namely the eigenvector corresponding to the largest eigenvalue of $\mathbf{X}$. The projections of the original variables (i.e., the histograms) onto the first PC are called "scores". The first PC represents the metric to characterize surface patterns of the captured solidified layer micrographs.

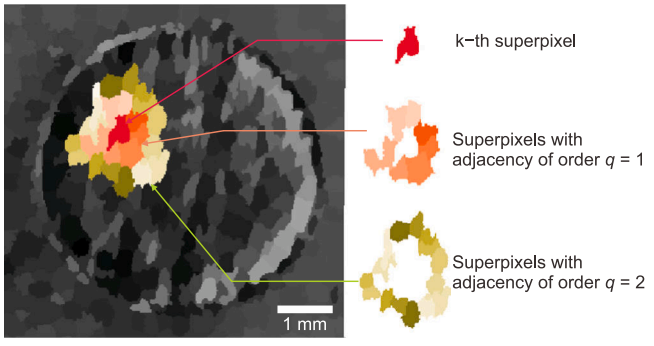

Fig. 2. Example of one superpixel and neighbor superpixels with adjacency of order 1 and 2.

The computation of the second salient attribute of superpixels—the image focus level—relies on the algorithm proposed by [35]. The main steps in this algorithm include:

1) Applying a low-pass filter to a given region of interest of the image (e.g., the k-th superpixel or a larger ROI including also adjacent superpixels),
2) Estimating intensity variations between neighboring pixels in the original image (in terms of absolute differences),
3) Estimating intensity variations between neighboring pixels in the low-pass filtered image (in terms of absolute differences),
4) Comparing the extent of site-specific intensity variations in the two micrographs. If the local difference is large, then the original image is in focus. Otherwise, the smaller the difference, the lower the focus level (i.e., the higher the blurriness) in the original image.

The resulting focus level ranges between 0 and 1, with 1 corresponding to the highest blurriness. Fig. 3 shows a schematic of the proposed approach to synthesize the information enclosed in the superpixels into a bi-variate space defined by the two descriptors—the first PC of histogram data and the focus level.

In summary, upon obtaining the SLIC-based superpixel segmentation for the current solidified layer, we reduce the dimensionality by grouping pixels into P_j superpixels and only consider two attributes: one which captures the superpixel blurriness and one which describes the intensity distribution both within the superpixel and among its neighbors, respectively. From a general implementation perspective, we suggest the computation of the two indices in a coherent way: if adjacent superpixels with adjacency order up to q are considered for the PCA analysis of the pixel intensity histograms, the blurriness index shall be computed on the adjacent superpixels with the same adjacency order.

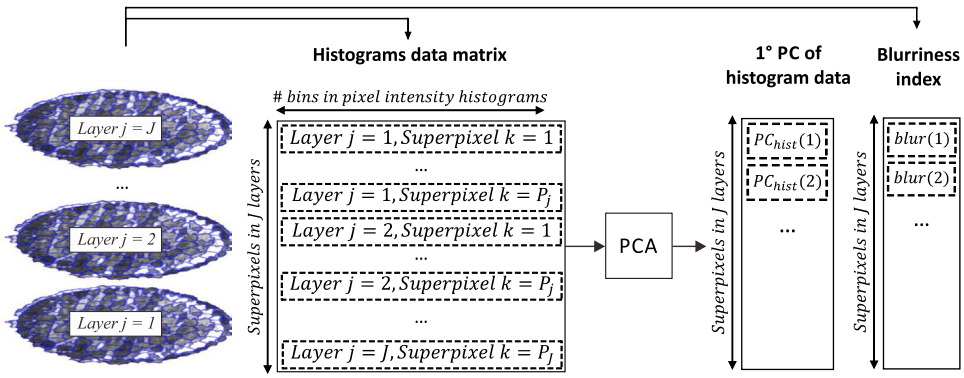

Fig. 3. Schematics of the proposed approach to estimate superpixel-level synthetic descriptors.

3. Experimental setup

We produced cylindrical specimens of AISI SS316L using powders from Höganäs AB with particle size distribution between 20 μm and 63 μm. Table 2 shows the powder chemical compositions. The production of specimens involved the use of a custom-built pulsed L-PBF system with integrated PBS that captures in-line, high-resolution micrographs of the solidified surface at each layer. The pulsed fiber laser source provides a maximum average power of 200 W at a central wavelength of 1065 nm. It also enables tuning the pulse shape in terms of frequency and pulse duration. The cylinders measured 5 mm in height and 5 mm in diameter. We produced three sets of cylindrical specimens, referred to as set A, set B, and set AR. The only difference between set A and set B—which we processed in the same run—was the laser pulse shape: A and B, respectively. In these two sets, we varied average laser power and laser scanning speed, but kept all other parameters constant, including the serpentine laser scanning strategy with 67° rotation each layer, the hatch spacing of 120 μm, and the powder layer thickness of 40 μm. Table 3 summarizes the process parameters used to produce set A and set B specimens and Fig. 4 shows the specimens' locations on the substrate. We compute the volumetric energy density, *VED*, by:

$$VED = \frac{P}{vht}. \tag{2}$$

Here, P is the power (in W), v is the scanning speed (in mm/s), h is the hatch spacing (in μm) and t is the layer thickness (in μm).

We use set AR specimens as a validation of the results collected for set A and set B. First, we produced set AR in a different run and used slightly different laser parameters compared to set A, but similar *VED*. The AR set included four groups (I, II, III, and IV) of the same four specimens, each arranged in a different order across the substrate (see Fig. 5). The four specimens in each group differed in average laser power and laser scanning speed, but were produced using all other parameters constant, including the pulse shape A, the serpentine laser scanning strategy with 67° rotation each layer, the hatch spacing of 80 μm, and the powder layer thickness of 30 μm. Table 4 shows the four process parameters.

A direct comparison between set A and set B specimens allows us investigating the effects of *VED* and the laser pulse shape on build density. In our matrix of experiments (Tables 3 and 4), we covered a wide range of *VED* values, which yielded both under-melting and over-melting of powders. Moreover, changing the laser pulse shape from A to B provides a means to study the effects of laser pulse modulation on build density while keeping *VED* constant. Indeed, pulse frequency and duration for pulse shape A are 950 kHz and 261 ns, respectively, while for pulse shape B are 500 kHz and 508 ns, respectively. By comparing set A against set AR, we could also assess the accuracy and repeatability of the proposed methodology in predicting density of specimens based on surface topography, regardless of the nominal process parameters used to produce them or their position on the substrate and with respect to the flow direction.

To capture micrographs of the solidified layers during specimen production, we set the PBS acquisition resolution to 1200 1200 DPI, leading to a spatial resolution of ~20 μm/pixel. The time taken to capture one colored micrograph at this resolution was ~1 min. The contact image sensor (CIS) of the PBS is characterized by a working distance of 3 mm and a depth-of-field of about 100 μm. Fig. 4 and Fig. 5 are examples of powder bed micrographs acquired with the blade-mounted CIS. The figures also illustrate the recoating direction as well as that of the shielding gas flow. We carried out PBS measurements, and compare the resulting density predictions, for 10 and 30 layers starting from layer 80 (build height, $z = 3.2$ mm) for set A and set B specimens, and for 118 layers starting from layer 21 (build height, $z = 0.6$ mm) for set AR specimens.

We carried out Archimedes' tests to determine the final density of all the specimens and used these results as ground truth to evaluate the accuracy of our PBS-based predictions. We used a Mettler Toledo XS204 analytical balance to measure the mass of the cylinder in air and subsequently in ethanol as an auxiliary liquid. We repeated the measurement for each cylinder three times and report the average density.

We also carried out X-ray CT on set A and set B specimens to examine the size and distribution of defects in the specimens using the Bruker SkyScan 1173 system. The scanning settings included a voxel size of 8 μm, voltage of 130 kV, current of 62 μA, rotation step of 0.2° and frame averaging of 6. We used the NRecon and CTAn software to reconstruct and analyze the size and distribution of defects in the specimens respectively.

4. Results

4.1. Superpixel segmentation

We apply the SLIC algorithm to PBS micrographs by setting an average superpixel size S = 300μm. According to our sensitivity analysis, this value is appropriate for the different specimens we produced in our work. We detail how this parameter may affect the predictions in

Table 2
Chemical compositions of SS 316L powders.

Iron	Chromium	Nickel	Molybdenum	Manganese	Silicon	Oxygen	Carbon
Balance	16 – 18%	11 – 14%	2 – 3%	2%	1%	0.062%	0.03%

Table 3
Process parameters for set A and set B specimens.

Set	Cylinder	Average laser power P (W)	Scanning speed v (mm/s)	Hatch spacing h (μm)	Layer thickness t (μm)	Pulse shape	Energy density (J/mm^3)
A	1	100	200	120	40	A	104
	2	100	100				208
	3	200	200				208
	4	200	150				278
	5	200	100				417
	6	200	80				521
	7	200	50				833
B	1	100	200			B	104
	2	100	100				208
	3	200	200				208
	4	200	150				278
	5	200	100				417
	6	200	80				521
	7	200	50				833

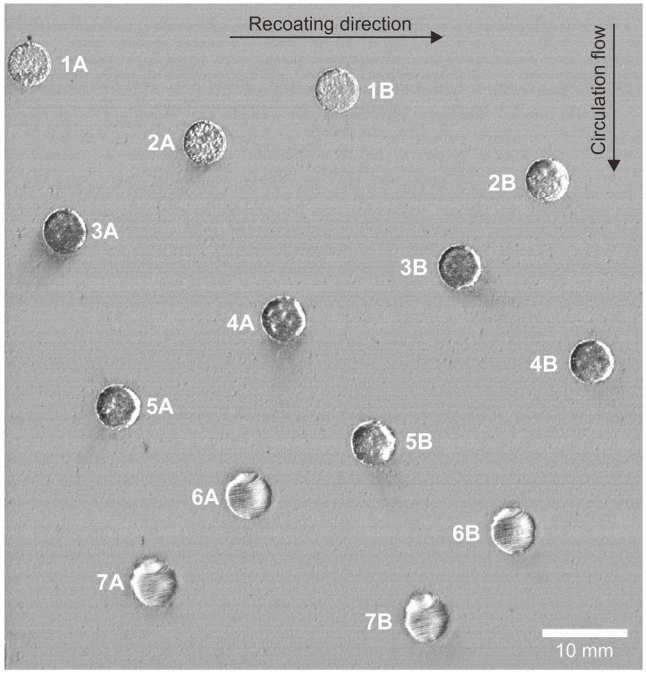

Fig. 4. PBS micrograph illustrating the arrangement of set A and set B specimens.

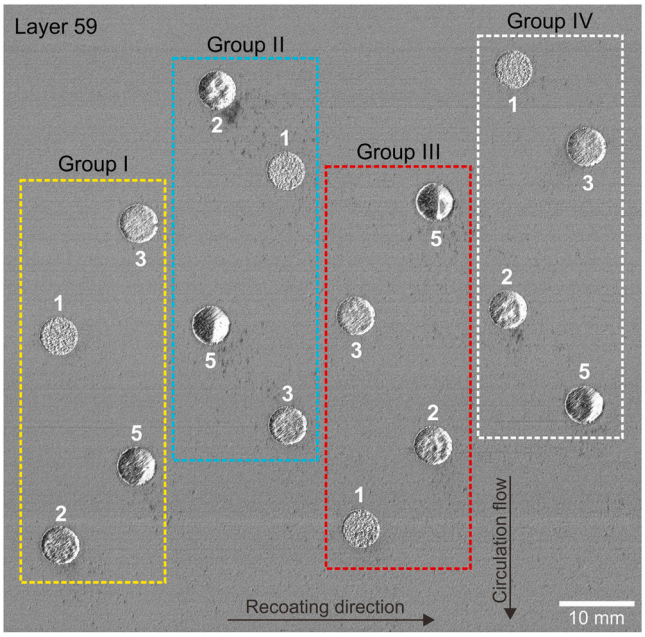

Fig. 5. PBS micrograph illustrating the arrangement of set AR specimens consisting of four groups of specimens (I, II, III and IV), produced using different process parameters (see Table 4).

Section 4.5. Fig. 6 shows the superpixel segmentation obtained by applying the SLIC technique to some representative solidified layers from specimens belonging to set A and set B. As observed in these two images, superpixels naturally adapt to the surface features of the solidified layer. For example, in specimen 1 from set A and set B (produced using a low *VED*)—the superpixel boundaries adapt to the presence of small dark and bright regions that correspond to small peaks and valleys. Conversely, in specimens 7 from set A and set B (produced using a high *VED*), some superpixels exhibit elongated geometries along the scan direction (since scan tracks are more clearly visible at higher energy input), while others have random orientation and globular shape.

4.2. Surface pattern descriptors

We employ three possible analysis methods to study how the two superpixel attributes we selected—based on intensity variations and local changes of the blurriness amongst neighboring superpixels—may be used to predict build density of set A and set B specimens. The methods are "Q2″, "weighted", and "no-weight". The Q2 method (i.e., adjacency order up to 2) consists of compiling the intensity histogram and blurriness level for pixels belonging to a ROI that is the union of the k-th superpixel and all adjacent superpixels up to $q = 2$. The weighted method consists of introducing a weight on the histograms which decreases as adjacency increases: $w = 1$ for the k-th superpixel with $q = 0$, $w = 0.5$ for superpixels with $q = 1$, $w = 0.25$ for superpixels with $q = 2$, and $w = 0$ for superpixels with $q = 3$. The no-weight method consists of computing the intensity histogram and the blurriness index of the k-th superpixel only, without including any information related to neighboring superpixels. We refer to this approach as the "no-weight" method, because is it equivalent to the weighted method with $w = 1$ for the k-th superpixel and $w = 0$ for all other superpixels. The rationale for using these three methods is to investigate whether the presence of defects—specifically porosity—in the build is related to variations in intensity and blurriness that are only local (i.e., within a superpixel) or distributed (across multiple superpixels).

Fig. 7 shows the pixel intensity histograms and the corresponding average histograms computed for the SLIC-based segmentation of one representative layer from different specimens belonging to set A (i.e., produced using different *VED*). The average intensity histograms (the solid red curves in Fig. 7) show that the three methods—Q2, "weighted", and "no-weight"—exhibit similar trends across the data set. By contrast,

Table 4
Process parameters for set AR specimens.

Group	Cylinder	Average laser power P (W)	Scanning speed v (mm/s)	Hatch spacing h (μm)	Layer thickness t (μm)	Pulse shape	Energy density (J/mm^3)
I / II / III / IV	1	100	500	80	30	A	83
	2	150	400				156
	3	180	550				136
	5	200	200				417

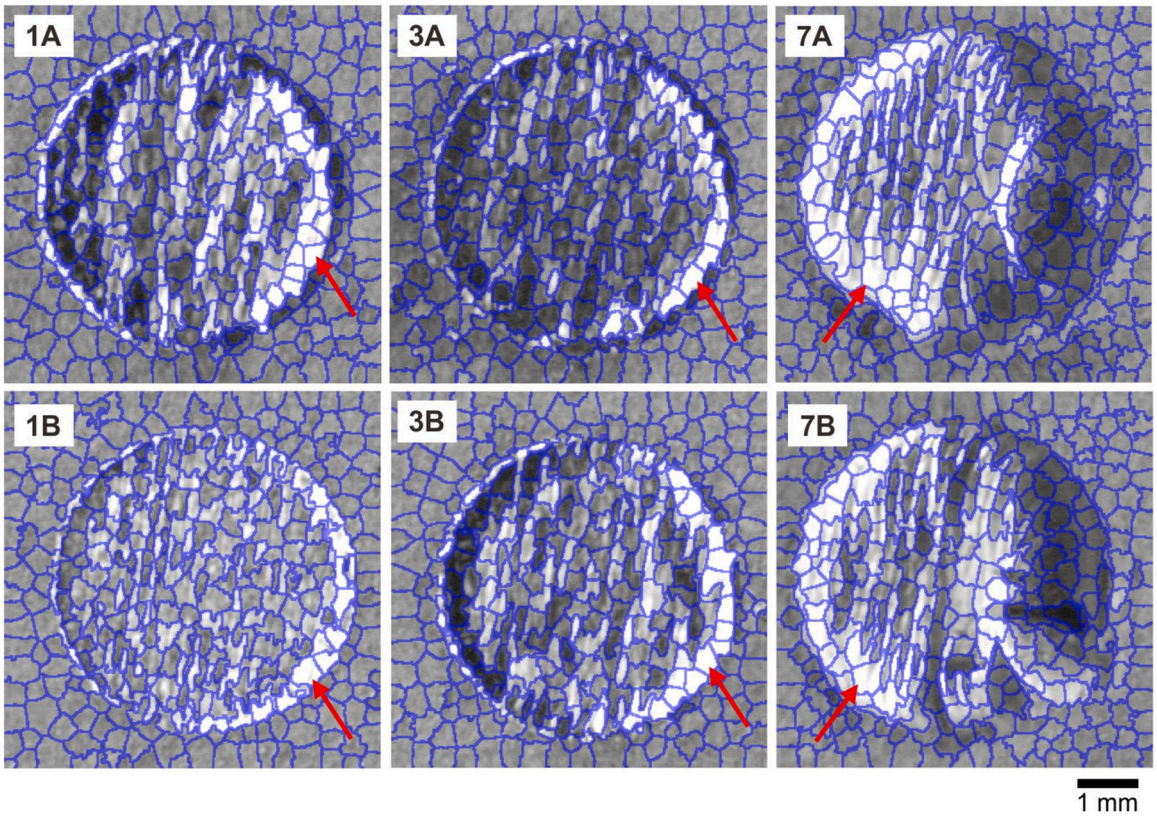

Fig. 6. SLIC-based segmentation (setting $S = 300\,\mu m$) on individual layers from specimens 1 A, 3 A, 7 A, 1B, 3B and 7B. The red arrows indicate saturated pixel regions near the contours.

there is a large difference in the variability of the pixel intensity histograms; especially when comparing the no-weight method against the Q2 and the weighted methods. There is a notable peak in Q2 and weighted histograms, while those corresponding to the no-weight method shows a much higher variability. Indeed, the Q2 and weighted methods can be viewed as weighted moving averages, which reduce the variability of the estimated quantity. Fig. 7 also indicates that different *VED* values yield different intensity histogram patterns. At the energy density that corresponds to the highest part density (specimen 3A), intensities exhibit a unimodal distribution, where only a few pixels are saturated and mainly distributed along the contours of the ROI (as shown in Fig. 6). By contrast, the intensity histograms of specimens 1 and 2 from sets A and set B —corresponding to low *VED*—exhibit a bimodal distribution (i.e., they include superpixels with both low and high intensity). At higher energy densities (specimens 4–7 of set A and set B), the bimodal distribution becomes even more evident. In these extreme cases, there exist a higher fraction of saturated superpixels (which is also visible from Fig. 5).

Following the methodology outlined in Section 2.2, we applied PCA to this dataset considering groups of histograms coming from 10 consecutive layers. The rationale behind the use of such a small number of layers in our analysis consists of showing that layerwise measurements in a few layers—combined with our proposed approach—is sufficient to obtain reliable estimates of build density. The results are depicted in Fig. 8. The loadings of the first PC can be thought of as weights assigned to different intensity values. The percentage of explained variance, which we report in the plot, can be thought of as the amount of information captured by the PC. Both Q2 and weighted methods exhibit comparable results. The Q2 method (the orange line in Fig. 8) suggests that the largest portion of variability (about 42%) can be explained in terms of intensity contrast between $I < 150$ and $I > 150$ (with a peak at saturation $I = 255$). The weighted method (the green line in Fig. 8) shows that the first PC has the same interpretation and about the same explained variability as the Q2 method (it is worth recalling that the sign of the loading is not relevant). The no-weight method (the grey line in Fig. 8) indicates that not considering superpixel adjacency results into a much lower explained variance (about 26%) and in significantly different loading compared to the foregoing case. Here, pixel intensities up to $I = 75$ (darker regions) are associated to zero-value loading and the first peak occurs at about $I = 140$ (as opposed to $I \approx 80$). Nevertheless, we notice a significant contrast between lower and higher intensities.

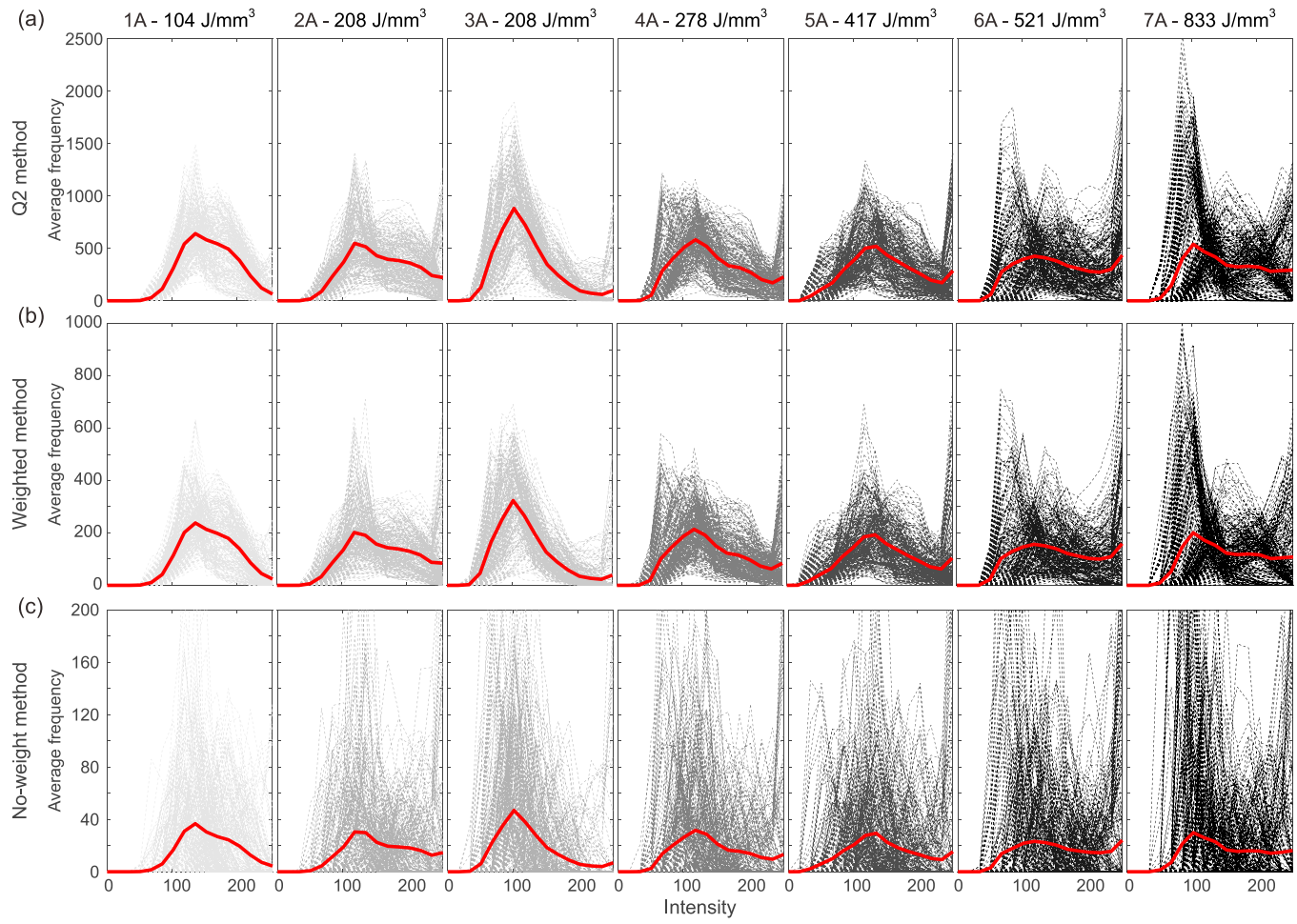

Fig. 7. Intensity histograms plotted using the Q2, weighted, and no-weight methods. The histograms refer to representative individual layers from specimens belonging to set A and produced using different *VED*s (whose values are reported on top of each plot). The respective average in each histogram appears as a solid red curve. The shade of grey used for the histograms scales with *VED*.

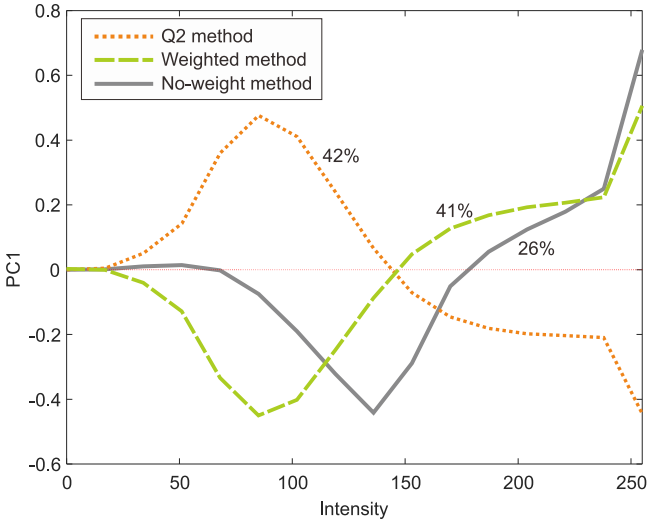

Fig. 8. Loading of the first PC computed considering histograms from 10 consecutive layers using the Q2, weighted, and no-weight methods for set A and set B specimens. The percentages indicate the explained variance of each method.

4.3. Density measurements and porosity analysis on set A and set B specimens

We measured the densities of set A and set B cylinders based on

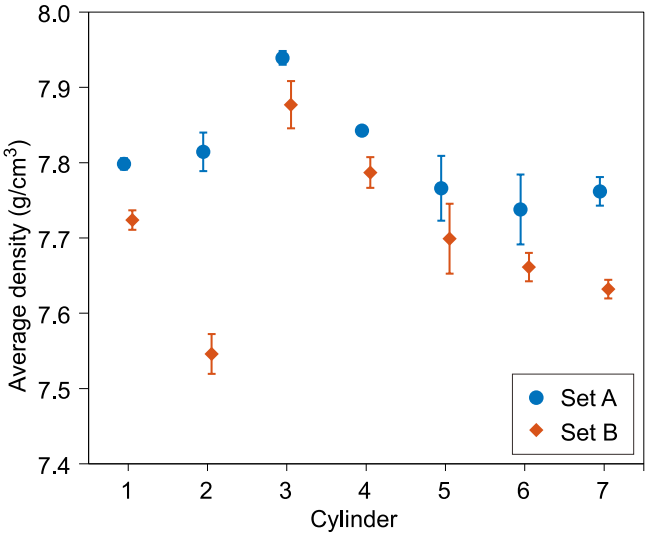

Fig. 9. Average density of set A and set B specimens.

Archimedes' principle and report their average readings in Fig. 9. The density of specimens belonging to set B is lower compared to that of the corresponding specimens in set A across all *VED* used. Since the only difference between these two sets of samples is the laser pulse shape employed, we attribute the lower density of set B specimens to the combination of frequency and pulse duration used. Specimens 3A and 3B ($P = 200$ W, $v = 200$ mm/s, $E = 208$ J/mm^3) are those exhibiting highest density in both sets. Interestingly, specimens 2A and 2B have significantly lower density (2B has the lowest amongst all specimens produced) although they have the same energy density ($E = 208$ J/mm^3)—achieved by lowering both laser power and scanning speed ($P = 100$ W and $v = 100$ mm/s).

We gathered more insights into the different types of porosity in set A and set B specimens using X-ray CT analysis. The results, in Fig. 10, show large and irregular lack-of-fusion pores with un-melted powder particles entrapped in specimens produced with the lowest energy density (specimens 1A and 1B). Increasing to $VED = 208$ J/mm^3 mitigates the porosity (specimens 2A and 2B), although small spherical pores that are aligned along the scan direction are still noticeable—especially in specimen 2B. Using the same energy density but increasing both laser power and scanning speed leads to the highest density in our dataset (specimens 3A and 3B). The cross section of some specimens is also seen in Fig. 11. We note that specimen 3A has lower porosities compared to the other specimens. Another finding is that keyhole and gas-entrapment porosity are particularly evident in specimens 5, 6, and 7 of set A and set B, where their $VED > 208$ J/mm^3. These features are, again, more prominent in set B.

4.4. Part density predictions of set A and set B specimens through PBS measurements

We refer to the scores of the first PC computed on the intensity histograms in Fig. 8 as PC_{hist}. Fig. 12 shows the scatter plot of PC_{hist} and blurriness value, *blur*, against the final part density for the Q2, weighted, and no-weight methods in both set A and set B specimens. All values consider measurements coming from $J = 10$ consecutive layers (from layer 80–90). Fig. 12 (a) shows a clear linear trend between the PC_{hist} values and the final specimen density, which is more evident for the Q2 and the weighted methods. By contrast, the larger variability of the PC_{hist} index in the no-weight method prevents any correlation to build density. The correlation is positive for the Q2 method and negative for the two other techniques simply because of the signs of PC loadings shown in Fig. 8.

Fig. 12 (b) shows that a higher blurriness corresponds to a lower specimen density. This correlation can be rationalized as follows. A rougher surface topography yields large *blur* values because surface asperities fall outside the CIS's depth of focus. This corrugation is probably caused by an unstable melt pool, which may lead to non-uniform solidification and generate defects [36]. Interestingly, the variability of the *blur* index obtained with the Q2 and weighted methods is lower than in the case where superpixel adjacency is not considered. This result suggests that *blur* variations within a larger area are more relevant for the prediction of build density. If neighboring superpixels have similar blurriness, the surface is likely to be flat and regular. Similar to the measured intensity variations, the Q2 and weighted methods can be thought of as weighted moving averages of *blur* values, which reduce their variability.

The PC_{hist} values are based on a linear combination of intensity histograms, which, as shown in Fig. 8, mainly captures the contrast between low and high intensities. As a result, a highly positive value of PC_{hist} in the Q2 method corresponds to a relatively homogeneous surface pattern with predominantly low intensity pixels. This pattern is representative of a regular surface resulting from a more stable and uniform solidification of the material, hence a higher build density. Zhu et al. [37] have shown that with sufficient energy input, the presence of voids and un-melted powder particles in the consolidate layer reduce significantly, resulting in parts with relatively high density and low roughness. By contrast, a large, negative value of PC_{hist} from the Q2 method corresponds to surface patterns with regions that exhibit high—and even saturated—intensity. These features are the result of severe process instabilities, where asperities in the surface topography may also cause strong out-of-plane distortions in the monitored layers. When the energy input is too low, the consolidated layer is non-uniform due to the presence of un-melted particles, which affect the interaction between the laser and the powder bed. Thus, the surface exhibits high roughness. When the energy input is too high, the surface tension of the melt pool is reduced and gives rise to ripples and irregularities, which remain frozen upon rapid solidification, resulting in poor surface quality [36]. Because the signs of PC loadings for the weighted and no-weight methods are opposite to that of the Q2 method, a large, negative value of PC_{hist} in this case corresponds to a relatively homogeneous surface pattern and a build of higher density.

In order to use the PC_{hist} and *blur* indices as predictors of the final build density, we fit a linear model to the density measurements obtained using Archimedes' method and present the results in Fig. 13. The Q2 approach yielded the highest goodness-of-fit ($R^2_{adj} = 0.805$). Table 5

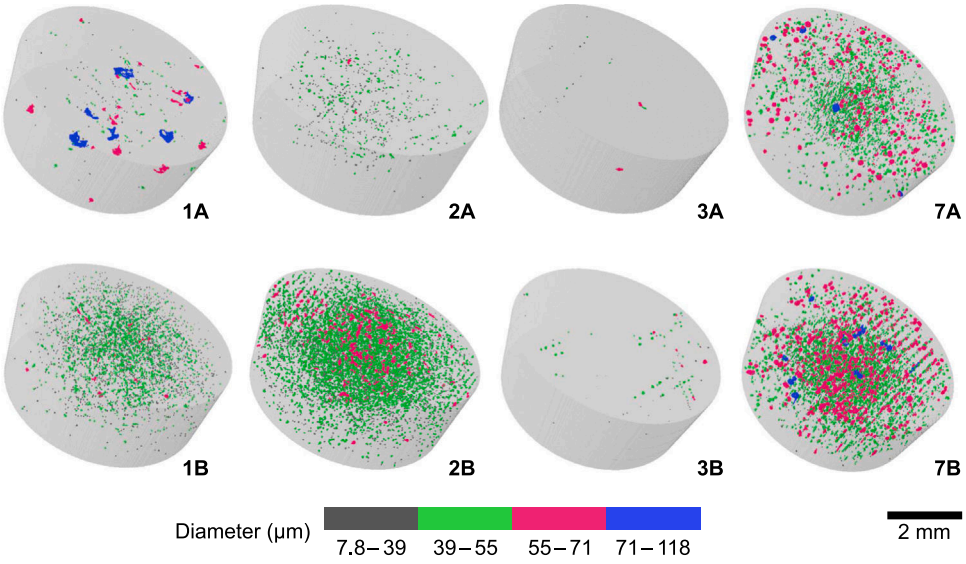

Fig. 10. CT models of specimens 1, 2, 3, and 7 from set A and set B.

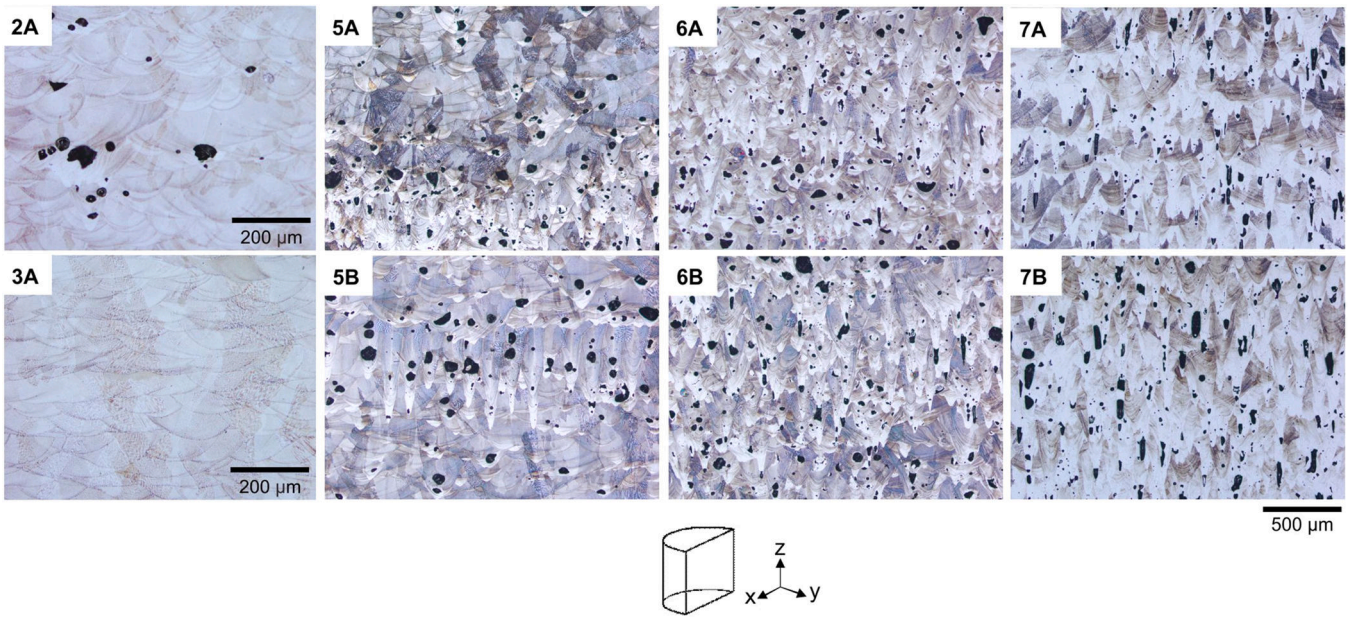

Fig. 11. Cross-section images from the $x-z$ plane of specimens 2A, 5A, 6A, 7A, 3A, 5B, 6B, and 7B.

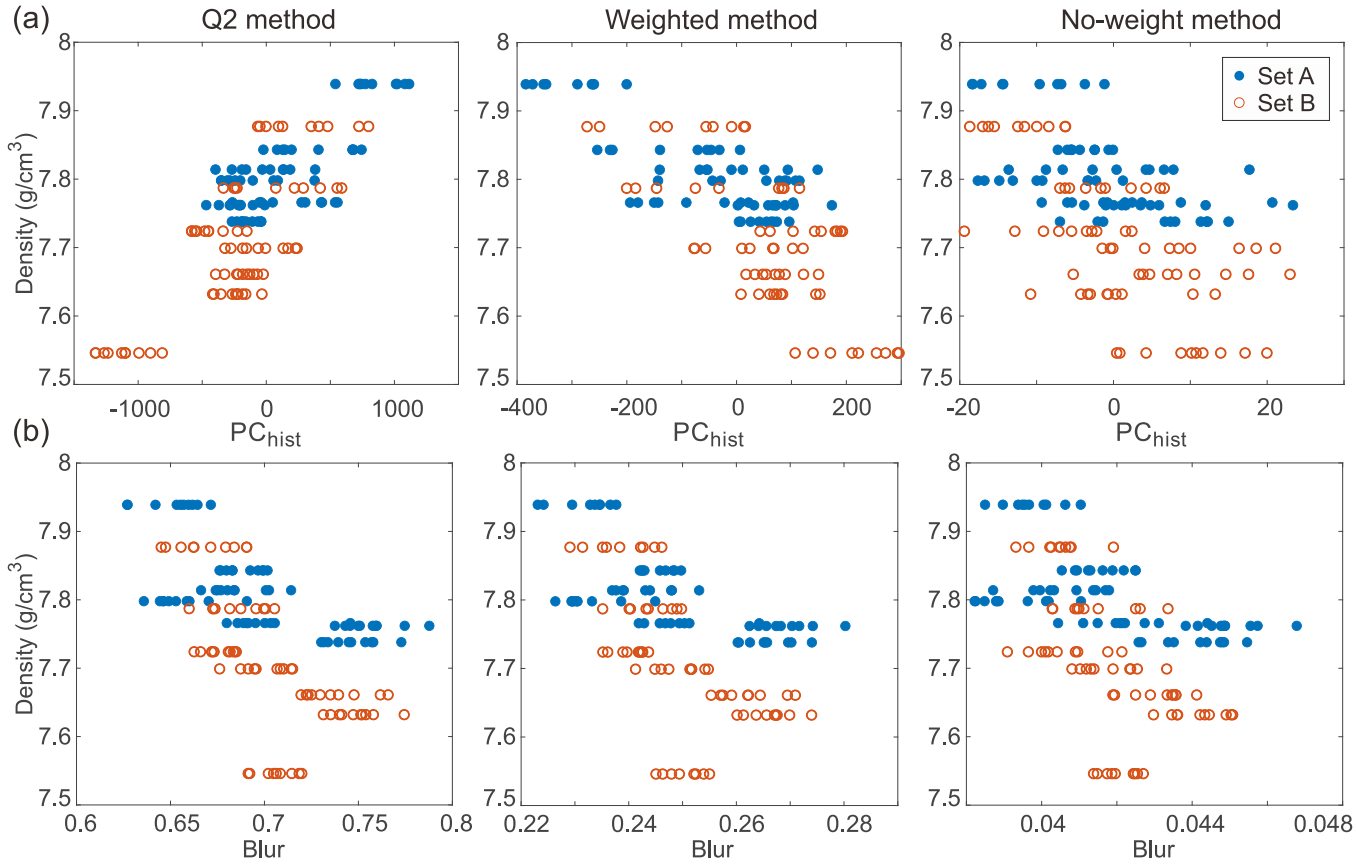

Fig. 12. Scatter plot of PC_{hist} and *blur* against density of specimens in set A and set B using the Q2, weighted, and no-weight methods.

shows the standardized effects associated with the two regressors, PC_{hist} and *blur*. All model terms are statistically significant to a 95% confidence level. By comparing these values, we ascribe the relative contribution of each regressor to the overall model. This analysis indicates that *blur* becomes less important with the transition from Q2 method (where the blurriness accounts for about half of the contribution of PC_{hist}) to the weighted and to the no-weight method (where the blurriness does not contribute to the model in a statistically significant way). From Fig. 13 and Table 5, we thus conclude that the Q2 method yields the best prediction performance amongst the methods considered.

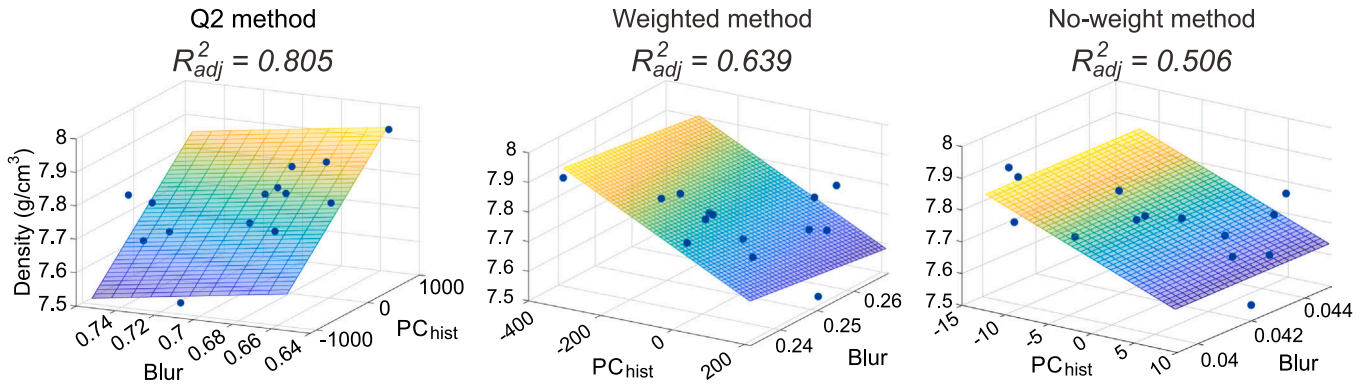

Fig. 13. Fitted model surface to density measurements of set A and set B specimens using the Q2, weight, and no-weight methods (plotted points correspond to specimens' density values).

Table 5
Linear model formulation, standardized effects and goodness of fit for different weighting schemes.

Method	Model	Standardized effects		Goodness-of-fit (R^2_{adj})
Q2	$Density = 8.326 + 1.74e^{-4}PC_{hist} - 0.801Blur$	PC_{hist}	5.649	0.805
		$Blur$	2.09	
Weighted	$Density = 8.167 - 6.22e^{-4}PC_{hist} - 1.649Blur$	PC_{hist}	4.898	0.639
		$Blur$	1.270	
No-weight	$Density = 7.746 - 0.011PC_{hist} + 0.211Blur$	PC_{hist}	2.842	0.506
		$Blur$	0.013	

4.5. Accuracy estimation and sensitivity analysis

To assess the prediction accuracy of our PBS-based in-line monitoring technique when using the Q2 method, we performed a leave-one-out cross-validation analysis by fitting the model using data from 13 out of 14 specimens (from set A and set B) and measuring the prediction error for the excluded one. We estimate the accuracy of predictions fitted onto measurements by means of the root mean square error (RMSE). The results, reported in Table 6, show that our method yields a RMSE value of 0.0510. This number comes from iterating the leave-one-out analysis 14 times, by selecting a different test specimen each time.

To compare the accuracy of predictions obtained with and without SLIC-based segmentation and to benchmark our methodology against other algorithms which were previously proposed in the literature [38], we analyzed our experimental dataset (i) without any prior segmentation of the images and (ii) considering surface roughness as the sole regressor. The first technique (hereafter referred to as the "no segmentation-based" method) consists of computing the same proposed surface pattern descriptors (PC_{hist} and $blur$) using the entire solidified layer of the specimen as ROI without any superpixel segmentation. By comparing the Q2 method against this technique, we demonstrate the benefit of estimating local descriptors through the SLIC-based segmentation rather than simply measuring an overall index. The second technique (hereafter referred to as the "areal roughness-based" method) consists of computing more traditional image-based areal roughness indices, such as the average roughness S_a and the root mean square roughness S_q [38]. We measure these quantities using the entire solidified layer of the specimen as ROI, without any superpixel segmentation. The reader is referred to [38] for details on the image-based computation of such indices. This second technique is deemed representative of benchmark methods aimed at investigating the correlation between the surface topography and part density.

Table 6 shows the comparison between the Q2 method and the two other approaches in terms of the leave-one-out RMSE. It also shows the resulting prediction error both for all specimens (set A and set B combined) as well as separately, for specimens belonging to set A and set B. Table 6 shows that the Q2 method outperforms the other two, yielding an RMSE that is about 33% lower than the one obtained by computing PC_{hist} and $blur$ on the entire solidified area without any superpixel segmentation (no segmentation-based method) and about 45% lower than the one obtained by using benchmark image-based areal roughness indices.

As mentioned in Section 2.1, the proposed method relies on the selection of a suitable value of S—through the choice of P—which sets the spatial resolution and defines the number of superpixels used in our algorithm. We performed an analysis to evaluate the sensitivity of the prediction accuracy and performance on the parameter S. The results presented in the foregoing sections were based on $S = 300\ \mu m$. We chose this value to demonstrate the ability to characterize the overall solidification pattern produced by L-PBF. Specifically, 300 μm roughly corresponds to twice the hatch distance. We repeated the analysis using $S = 125\ \mu m$ (i.e., equal to the hatch distance) and $S = 600\ \mu m$ to investigate the effect of this variable on our method and the resulting density predictions. The results are presented in Table 7.

When using a larger superpixel size, the resulting RMSE in the prediction of final part density approaches the one obtained with the no segmentation-based method (see Table 6). By contrast, when using a smaller S, over segmentation may occur, which yields a slight reduction of prediction accuracy with respect to the proposed settings (i.e., $S = 300\ \mu m$). As a general guideline, we recommend selecting an

Table 6
Leave-one-out cross-validation RMSE for the Q2 method and the two other techniques for all specimens (overall) and specimens belonging to set A and set B respectively.

Method	$RMSE(g/cm^3)$		
	Set A	Set B	Overall
Q2 method	0.0543	0.0475	0.0510
No segmentation-based method	0.0721	0.0783	0.0753
Areal roughness-based method	0.0947	0.0897	0.0923

Table 7
Leave-one-out cross-validation RMSE for different approximate superpixel sizes for all specimens (overall) and specimens belonging to set A and set B respectively.

Approximate superpixel size (μm), S	$RMSE(g/cm^3)$		
	Set A	Set B	Overall
125	0.0671	0.0703	0.0688
300	0.0543	0.0475	0.0510
600	0.0670	0.0786	0.0730

approximated size of superpixels that is twice the hatch distance to avoid over and under segmentation of surface features that characterize the surface patterns. In the present case study, with a lateral resolution of the input image of 20 μm/pixel, a size S between two and three times the hatch spacing is the one that provides the best prediction performance. We recommend selecting S in this range when the acquired images or scans have spatial resolution analogous to (or even higher than) the one used in this work. Moving from $S = 125\,\mu m$ to $S = 600\,\mu m$ yields no significant change of the computational time needed to carry out the SLIC-based segmentation. In the present study, the SLIC algorithm (implemented in MATLAB) required on average 0.12 s to perform the segmentation of solidified layers on a regular laptop equipped with an Intel® core i7 processor. The full processing time per layer includes the acquisition time of one micrograph, which is ~1 min at 1200 DPI, and the time to compute the proposed descriptors (Q2 method) for all solidified surfaces, which is ~0.4 s/mm^2. The latter includes only the area of the solidified cylinders, i.e., after the application of binary mask onto the ROI, and not the entire powder bed.

We also carried out an additional investigation to assess how the number of PBS-acquired micrographs (i.e., the number of measured layers) affects the resulting regression model to estimate build density. In the foregoing sections, we present results based on using 10 consecutive layers to fit the models, as shown in Fig. 13 and Table 5. Fig. 14 and Table 8 show how the predictions change when considering PBS-acquired micrographs from 30 consecutive layers.

From this data, it appears that the correlation between both PC_{hist} and *blur* descriptors and build density is confirmed when using 30 layers (i.e., the model coefficients are not statistically different). Clearly, using more measurements will provide more accurate predictions at the cost of data processing speed. To demonstrate this point, we apply our methodology to the entire dataset AR and present the results in the following Section 4.6. This analysis took ~12-times longer compared to when using only 10 layers and led to a similar outcome on build density prediction, i.e., the predictions are in good agreement between in-situ and ex-situ density estimates. From an in-situ monitoring perspective, analyzing a few consecutive layers can be a reasonable compromise to quickly detect major deviations from a target process condition. From a process optimization perspective, instead, larger batches of consecutive layers could be needed to decide whether a given set of process parameters needs be screened out. We speculate that using more images in the analysis could even help identify individual porosity defects across the build. However, the main goal of our methodology is to establish a global correlation between in-situ and ex-situ estimates rather than providing an accurate mapping of defects within builds. In this context, using fewer images is enough to acquire statistically representative

Table 8
Comparison of part density estimation models based on measurements performed in 10 and 30 consecutive layers for set A and set B specimens.

Number of layers	Model	Standardized effects		Goodness-of-fit (R^2_{adj})
10	$Density = 8.326 + 1.74e^{-4}PC_{hist} - 0.801Blur$	PC_{hist}	5.649	0.805
		Blur	2.09	
30	$Density = 8.309 + 1.75e^{-4}PC_{hist} - 0.777Blur$	PC_{hist}	5.263	0.778
		Blur	1.86	

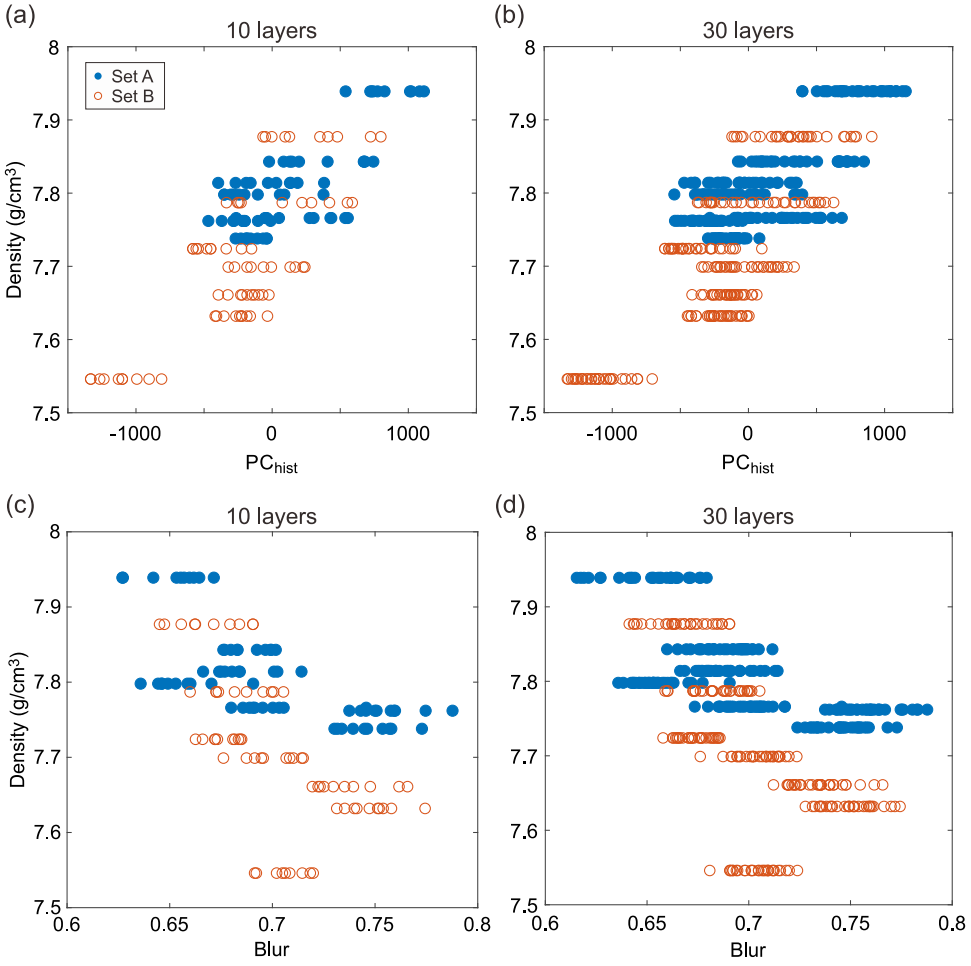

Fig. 14. Scatter plot of PC_{hist} and *blur* against the part density of specimens in set A and set B for 10 and 30 measured layers.

surface conditions during melting and solidification and provide accurate build density estimates. While porosities may not be evenly distributed within parts (as it is the case for specimens 5, 6, and 7 from set A and set B), the mechanisms by which they may form are likely to be at play throughout the entire build. Sometimes they may just not yield a defect. However, they may still impart measurable differences in the surface patterns across all layers. That enables our methodology to provide accurate estimates of build density even without using images from layers that actually contain porosity defects. All in all, these results demonstrate that gathering in-situ measurements from a few consecutive layers is sufficient to identify a statistically significant correlation between the solidified layer pattern and the final part density. That is if parts geometry and process parameters are kept constant each layer.

4.6. Validation experiment using the AR set

The AR set specimens produced using four different *VED* levels exhibit variable mean density values, as illustrated in Fig. 15. Specimens 1 correspond to a lack-of-fusion condition, specimens 2 and 3 correspond to high-density parts, and specimens 5 correspond to a key-hole porosity condition. There is no significant difference in part density between specimens 2 and 3 in spite of the different *VED* used (156 J/mm^3 and 136 J/mm^3, respectively). By contrast, there is a statistically significant difference in part density between specimens with lack-of-fusion porosity (*VED* of 83 J/mm^3) and keyhole porosity (*VED* of 417 J/mm^3). We also note that specimens 5 exhibit larger part-to-part variability; probably due to the use of a relatively large *VED*, which induces violent convection currents and strong vapor recoil forces that could erratically disrupt the melting process.

We apply the Q2 method to analyze PC_{hist} and *blur* from the AR set specimens. We use the same linear model shown in Table 5 (Q2 method) to infer density predictions for each specimen. To this end, we use the same PCA loadings that we estimate from set A and set B (shown in Fig. 8) to compute the PC_{hist} descriptor for set AR specimens. This implies that we project the measurements of set AR specimens onto the previously estimated PC direction, enabling PC_{hist} computation in the validation experiment. In other words, we use the experiment described in Section 3 (involving set A and set B) as a "training set" to estimate the intensity histograms and the linear model for build density prediction of set AR specimens. Fig. 16 illustrates the 95% confidence intervals of mean density predictions drawn by measuring 118 consecutive layers of the validation build, i.e., across all the PBS-acquired micrographs.

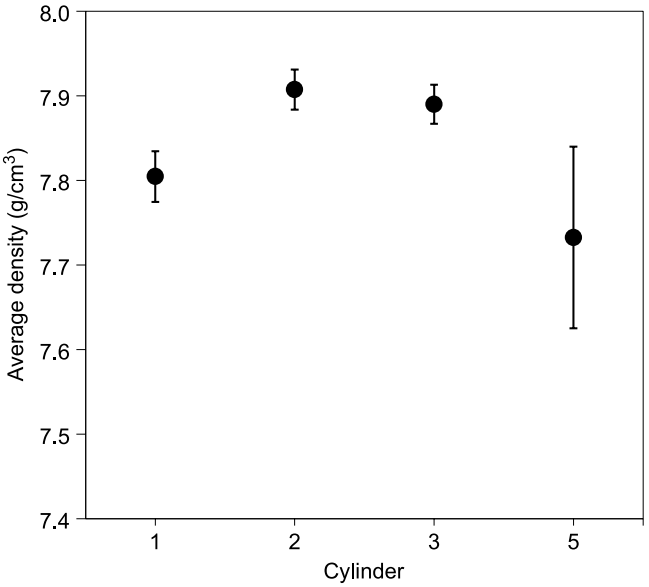

Fig. 15. Average density of set AR specimens.

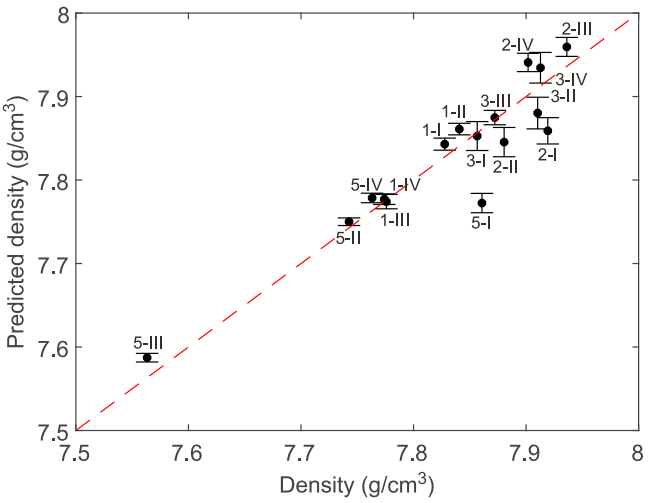

Fig. 16. Comparison between reference density measured via Archimedes' method and the predicted density enabled by the proposed approach. The plot shows the 95% confidence intervals of the sample mean predictions across 118 consecutive layers for set AR specimens.

Ideally, predictions should lay on the diagonal (red dashed line). Most datapoints (13 out of 16) do follow this ideal trend, suggesting a good agreement between in-situ and ex-situ density estimates. Moreover, for all the specimens in the AR set (with the only exception of specimen 5-I), the deviation between the mean predicted value and the reference value is lower than 0.05 g/cm^3. The most obvious outlier is specimen 5-I, which is characterized by keyhole porosity. Interestingly, this specimen detached from the substrate after 83 layers because of severe delamination. This result further supports our suspects on the large variability in part density of specimens 5 due to the high *VED* used. This process instability may have led to a build with significantly different surface compared to what a nominal specimen 5-I should be. Fig. 16 shows that specimens having significantly different densities are also associated with significantly different predictions according to the proposed approach. This observation has important practical implications, since it may be interesting to detect a deviation from a target condition that affects a specific portion of the build.

In summary, the results from this validation experiment show that: (i) analyzing all the micrographs (entire dataset) yields similar outcome on build density prediction as compared to a few consecutive layers (for set A and set B specimens), (ii) the correlation between in-situ modelled surface patterns is consistent across different builds, (iii) process conditions that produce statistically different density conditions also produce statistically different predictions based on in-situ measured descriptors, and (iv) the prediction accuracy and the associated uncertainty are appropriate to identify and classify deviations from a target density condition relying on in-situ measurements from a few consecutive layers.

5. Discussions

The results shown in Section 4 demonstrate that the proposed method allows an accurate prediction of the build density by using two synthetic indices, which may be estimated in-situ and from a few consecutive layers. The Q2 method provides more accurate predictions of final part density compared to the other two methods, which put lower weight on information coming from adjacent superpixels. The higher performance of this method is confirmed by a distinct linear trend between the PC_{hist} values and the final specimen density as shown in Fig. 12 (a), which is indeed more evident when using the Q2 method. The larger spread in PC_{hist} values for the no-weight method concealed the correlation to the final density. The RMSE values in Table 6 are a

measure of the prediction uncertainty. Each superpixel corresponds to a small region of the micrograph with relatively homogeneous pixel intensities within itself. These results suggest that inferring part density from surface topography requires the analysis of more distributed features, as opposed to just the local characteristics of the surface. This also implies that defects in the build either disrupt, or are the product of instabilities related to, the melting and solidification of the alloy from a greater volume compared to the defects' physical extension. The Q2 method yields a RMSE of 0.051 g/cm^3, which corresponds to 0.66% of the mean density of the specimens produced in our first experimental dataset, i.e., set A and set B specimens. This value illustrates that the uncertainty in the estimates of build density is relatively small. Thus, our method allows distinguishing builds that have relatively small differences in density.

The two descriptors we propose in this work are suitable to capture and model surface topographies that range from regular and flat patterns (associated with high build density) to various kinds of surface irregularities (associated with lower densities). However, it is important to note that predictions based these descriptors require analysis from a number of consecutive layers. If surface irregularities are limited to individual layers, they may not be representative of build quality. In this work, we found the PC_{hist} descriptor—which quantifies the pixel intensity distribution within sub-portions of the solidified layer—to be the most significant predictor. Adding the *blur* descriptor enabled by the unique capabilities of the PBS technology brings additional—and complementary—information about build density (when using the Q2 method). Indeed, a higher blurriness corresponds to a lower specimen density, as illustrated in Fig. 12 (b). Interestingly, however, specimen 2B—which exhibits the lowest density across our experimental data set—does not exhibit the lowest *blur* value. This apparent discrepancy may be due to the fact that porosity defects in specimen 2B are not related to the surface topography of the correspondent layers. These specific defects have diameter ranging between ~40 μm and ~55 μm and are aligned along melt tracks as shown in the CT model of Fig. 10. We speculate that they may form highly localized mechanisms (e.g., the result of gas entrapment within the melt pool as the liquid metal vaporizes), which do not produce significant perturbations on the metal surface, thus leading to too low variations in PC_{hist} and *blur* to be identified. As such, they may be considered as example defects/instabilities which cannot be resolved using our PBS-based method. Because both *blur* and PC_{hist} are related to the surface topography—the first is a direct assessment of intensity variations stemming from the presence of asperities on the surface, while the second is an indirect assessment of their height—it may be tempting to believe that they are redundant. Indeed, the results in Fig. 12 and Table 5 show that the two parameters are correlated. However, they are statistically significant and thus both contribute to a different extent to the overall information. As a result, build density evaluation based on both descriptors is deemed more accurate than relying exclusive on either of them.

It is worth recalling that, in the experiment discussed in Section 3, set A and set B employed the same energy density, yet they exhibited different density. While a density prediction based exclusively on *VED* would not capture these differences in the dataset, our methodology correctly quantifies and distinguishes the density from these two sets of specimens. The implications of this result are quite intriguing as our methodology can differentiate the density of builds based on differences in their percentage volume of porosity. Using this same argument, we elucidate the differences between specimens 2A, 2B, 3A and 3B, produced using the same energy density but different combinations of laser power and scanning speed. As a result, specimens 2A and 3A exhibit higher density compared to specimens 2B and 3B respectively. Several studies have shown that *VED* is not the only factor to be considered when analyzing the formation of defects in—or inferring the density of—parts produced by L-PBF [39,40]. For instance, Prashanth et al. [40] showed that the density of Al-12Si alloy parts produced by L-PBF scales with laser power and scanning speed even when keeping *VED* constant. This trend is in agreement with our results (as seen in Fig. 9). According to Bertoli et al. [39], a higher laser power has a more dominant effect on the melting regime than a reduction in scanning speed. The increase in laser power causes an increase in the maximum temperature reached in the powder bed, ensuring the complete melting of powder particles in specimen 3A.

6. Conclusions

The analysis of the signals captured during in-situ monitoring of AM processes are typically difficult to interpret. Here, we present a fast, cost-effective and versatile method to understand simple surface images. Leveraging on the PBS, we captured high-resolution (~20 μm/pixel) and large FOV micrographs of solidified areas of the layer, to which we applied SLIC-based superpixel segmentation. We then computed local variations of pixel intensity and local blurriness level within superpixels and used them as a proxy to quantify surface topography. By correlating this information with build density measurements obtained via Archimedes' method, we develop a model to predict the density of different specimens. We show that 13 out of 16 predictions are in good agreement between in-situ and ex-situ density estimates based on the analysis of 118 consecutive micrographs from the validation experiment. By extending the number of micrographs for the computation of the mean prediction from 10 to 30, the accuracy increases slightly. However, the image processing time scales directly with number of micrographs considered.

Our proposed methodology can accurately predict differences in density between parts produced with very similar *VED* but exhibiting different porosity levels. It captures the variations in pixel intensity within a relatively large area and has the lowest RMSE of 0.0510 as compared to other benchmark methods. However, our method should not be considered as an alternative to standard density metrology. In fact, it cannot provide a direct density measurement. The strength of the method lies in the capability to infer build density with a determined uncertainty range based on the correlation between the surface pattern that repeats layer by layer and the corresponding build density (measured ex-situ). Thus, it makes it possible to detect, in-line and in-situ, surface patterns that are not representative of a target density condition. The proposed methodology has potential for several different applications, ranging from in-situ monitoring of the L-PBF process to process optimization and material development procedures, where in-situ measurements may aid the reduction of the experimental effort. For in-situ monitoring, capturing differences between dense and very dense builds is most interesting, given that manufacturers typically already have established process parameters to produce high quality builds. However, identifying those process parameters is a time and resource intensive process, mostly based on trial and error. Using a cost-effective in-line monitoring method such as the one we present in this work could help in this endeavor substantially. Moreover, we would like to point out that defects in builds may occur stochastically, even when using optimized process parameters. For the most part, these defects are difficult to predict and to identify during the additive process. Even in these cases, we envision our method to be instrumental to avoid build failure or the production of parts with substandard performance.

We envisage several possible extensions and improvements of the proposed approach. It would be interesting to expand the analysis to include other superpixels attributes, which may provide insights into additional materials properties besides density. For instance, the morphology of superpixels could carry information about the underlying microstructure of the metals and metal alloys processed by L-PBF. Another field of research that our current work opens regards investigating how the relationships between build density and surface topography may change when producing parts with more complex geometries, which would be more representative of real-life parts. In this case, surface pattern variations would be also a function of the thermal distribution across the layer, which depends on the laser scan vector

[41] and local changes in the cross-sectional area of the features to be produced [42].

The success of our methodology opens new opportunities for achieving defect-free and more consistent builds. Because of the fast data acquisition and data analysis speed, anomalies may be detected and corrected on the fly, by the tuning the process parameters during the L-PBF process. Not only this paradigm would reduce experimental efforts to produce high quality builds, but also help make AM processes more sustainable, by improving the chances of successful builds and reducing material waste.

CRediT authorship contribution statement

Tan-Phuc Le: Writing – review & editing, Visualization, Software, Conceptualization. **Matteo Seita:** Writing – review & editing, Supervision, Project administration, Methodology, Funding acquisition, Conceptualization. **Qingyang Lu:** Writing – review & editing, Writing – original draft, Visualization, Validation, Investigation, Formal analysis, Conceptualization. **Marco Grasso:** Writing – review & editing, Writing – original draft, Visualization, Software, Methodology, Formal analysis, Conceptualization.

Declaration of Competing Interest

The authors declare that they have no known competing financial interests or personal relationships that could have appeared to influence the work reported in this paper.

Acknowledgements

This work was funded by the National Research Foundation (NRF) Singapore, under the NRF Fellowship program (NRF-NRFF2018-05) and supported by Nanyang Technological University (NTU). The authors would like to acknowledge Jude Emil Fonda from the Additive Microstructure Engineering (AddME) Lab at NTU for his help with sample production. Access to shared experimental facilities used in this work was provided by the School of Mechanical and Aerospace Engineering and the Singapore Centre for 3D Printing (SC3DP) at NTU.

References

[1] P. Yadav, O. Rigo, C. Arvieu, E. Le Guen, E. Lacoste, In situ monitoring systems of the SLM process: on the need to develop machine learning models for data processing, Crystals 10 (2020), https://doi.org/10.3390/cryst10060524.

[2] R. McCann, M.A. Obeidi, C. Hughes, É. McCarthy, D.S. Egan, R.K. Vijayaraghavan, A.M. Joshi, V. Acinas Garzon, D.P. Dowling, P.J. McNally, D. Brabazon, In-situ sensing, process monitoring and machine control in laser powder bed fusion: a review, Addit. Manuf. 45 (2021), 102058, https://doi.org/10.1016/j.addma.2021.102058.

[3] J. Lee, H.J. Park, S. Chai, G.R. Kim, H. Yong, S.J. Bae, D. Kwon, Review on quality control methods in metal additive manufacturing, Appl. Sci. 11 (2021), https://doi.org/10.3390/app11041966.

[4] M. Grasso, A. Remani, A. Dickins, B.M. Colosimo, R.K. Leach, In-situ measurement and monitoring methods for metal powder bed fusion: an updated review, Meas. Sci. Technol. 32 (2021), 112001, https://doi.org/10.1088/1361-6501/ac0b6b.

[5] M. Aminzadeh, T.R. Kurfess, Online quality inspection using Bayesian classification in powder-bed additive manufacturing from high-resolution visual camera images, J. Intell. Manuf. 30 (2019) 2505–2523, https://doi.org/10.1007/s10845-018-1412-0.

[6] Q.Y. Lu, N.V. Nguyen, A.J.W. Hum, T. Tran, C.H. Wong, Identification and evaluation of defects in selective laser melted 316L stainless steel parts via in-situ monitoring and micro computed tomography, Addit. Manuf. 35 (2020), 101287, https://doi.org/10.1016/j.addma.2020.101287.

[7] F. Caltanissetta, M. Grasso, S. Petrò, B.M. Colosimo, Characterization of in-situ measurements based on layerwise imaging in laser powder bed fusion, Addit. Manuf. 24 (2018) 183–199, https://doi.org/10.1016/j.addma.2018.09.017.

[8] S. Kleszczynski , J. Zur Jacobsmühlen , J.T. Sehrt , G. Witt , Error detection in laser beam melting systems by high resolution imaging, in: Proc. 23rd Annu. Int. Solid Free. Fabr. Symp., 2012.

[9] J. zur Jacobsmühlen , S. Kleszczynski , G. Witt , D. Merhof , Elevated region area measurement for quantitative analysis of laser beam melting process stability, in: Proc. 26th Annu. Int. Solid Free. Fabr. Symp., 2015: pp. 549–559.

[10] J. zur Jacobsmühlen, J. Achterhold, S. Kleszczynski, G. Witt, D. Merhof, In situ measurement of part geometries in layer images from laser beam melting processes, Prog. Addit. Manuf. 4 (2019) 155–165, https://doi.org/10.1007/s40964-018-0068-9.

[11] B.K. Foster, E.W. Reutzel, A.R. Nassar, B.T. Hall, S.W. Brown, C.J. Dickman, Optical, layerwise monitoring of powder bed fusion, in: Proc. 26th Annu. Int. Solid Free. Fabr. Symp., 2015.

[12] C. Gobert, E.W. Reutzel, J. Petrich, A.R. Nassar, S. Phoha, Application of supervised machine learning for defect detection during metallic powder bed fusion additive manufacturing using high resolution imaging, Addit. Manuf. 21 (2018) 517–528, https://doi.org/10.1016/j.addma.2018.04.005.

[13] M. Abdelrahman, E.W. Reutzel, A.R. Nassar, T.L. Starr, Flaw detection in powder bed fusion using optical imaging, Addit. Manuf. 15 (2017) 1–11, https://doi.org/10.1016/j.addma.2017.02.001.

[14] L. Pagani, M. Grasso, P.J. Scott, B.M. Colosimo, Automated layerwise detection of geometrical distortions in laser powder bed fusion, Addit. Manuf. 36 (2020), 101435, https://doi.org/10.1016/j.addma.2020.101435.

[15] L. Scime, D. Siddel, S. Baird, V. Paquit, Layer-wise anomaly detection and classification for powder bed additive manufacturing processes: a machine-agnostic algorithm for real-time pixel-wise semantic segmentation, Addit. Manuf. 36 (2020), 101453, https://doi.org/10.1016/j.addma.2020.101453.

[16] L. Scime, J. Beuth, A multi-scale convolutional neural network for autonomous anomaly detection and classification in a laser powder bed fusion additive manufacturing process, Addit. Manuf. 24 (2018) 273–286, https://doi.org/10.1016/j.addma.2018.09.034.

[17] W.S. Land, B. Zhang, J. Ziegert, A. Davies, In-situ metrology system for laser powder bed fusion additive process, Procedia Manuf. 1 (2015) 393–403, https://doi.org/10.1016/j.promfg.2015.09.047.

[18] B. Zhang, J. Ziegert, F. Farahi, A. Davies, In situ surface topography of laser powder bed fusion using fringe projection, Addit. Manuf. 12 (2016) 100–107, https://doi.org/10.1016/j.addma.2016.08.001.

[19] A. Dickins, T. Widjanarko, D. Sims-Waterhouse, A. Thompson, S. Lawes, N. Senin, R. Leach, Multi-view fringe projection system for surface topography measurement during metal powder bed fusion, J. Opt. Soc. Am. A 37 (2020) B93–B105, https://doi.org/10.1364/JOSAA.396186.

[20] M. Kalms, R. Narita, C. Thomy, F. Vollertsen, R.B. Bergmann, New approach to evaluate 3D laser printed parts in powder bed fusion-based additive manufacturing in-line within closed space, Addit. Manuf. 26 (2019) 161–165, https://doi.org/10.1016/j.addma.2019.01.011.

[21] T.G. Fleming, S.G.L. Nestor, T.R. Allen, M.A. Boukhaled, N.J. Smith, J.M. Fraser, Tracking and controlling the morphology evolution of 3D powder-bed fusion in situ using inline coherent imaging, Addit. Manuf. 32 (2020), 100978, https://doi.org/10.1016/j.addma.2019.100978.

[22] P.J. DePond, G. Guss, S. Ly, N.P. Calta, D. Deane, S. Khairallah, M.J. Matthews, In situ measurements of layer roughness during laser powder bed fusion additive manufacturing using low coherence scanning interferometry, Mater. Des. 154 (2018) 347–359, https://doi.org/10.1016/j.matdes.2018.05.050.

[23] L. Tan Phuc, M. Seita, A high-resolution and large field-of-view scanner for in-line characterization of powder bed defects during additive manufacturing, Mater. Des. 164 (2019), 107562, https://doi.org/10.1016/j.matdes.2018.107562.

[24] T.-P. Le, X. Wang, K.P. Davidson, J.E. Fronda, M. Seita, Experimental analysis of powder layer quality as a function of feedstock and recoating strategies, Addit. Manuf. 39 (2021), 101890, https://doi.org/10.1016/j.addma.2021.101890.

[25] F.G. Fischer, N. Birk, L. Rooney, L. Jauer, J.H. Schleifenbaum, Optical process monitoring in laser powder bed fusion using a recoater-based line camera, Addit. Manuf. 47 (2021), 102218, https://doi.org/10.1016/j.addma.2021.102218.

[26] C. Barrett, E. MacDonald, B. Conner, F. Persi, Micron-level layer-wise surface profilometry to detect porosity defects in powder bed fusion of Inconel 718, JOM 70 (2018) 1844–1852, https://doi.org/10.1007/s11837-018-3025-7.

[27] L. Scime, J. Beuth, Anomaly detection and classification in a laser powder bed additive manufacturing process using a trained computer vision algorithm, Addit. Manuf. 19 (2018) 114–126, https://doi.org/10.1016/j.addma.2017.11.009.

[28] Ren, Malik, Learning a classification model for segmentation, in: Proc. IEEE Int. Conf. Comput. Vis., 2003: pp. 10–17 vol.1. https://doi.org/10.1109/ICCV.2003.1238308.

[29] R. Achanta, A. Shaji, K. Smith, A. Lucchi, P. Fua, S. Süsstrunk, SLIC superpixels, 2010.

[30] R. Achanta, A. Shaji, K. Smith, A. Lucchi, P. Fua, S. Süsstrunk, SLIC superpixels compared to state-of-the-art superpixel methods, IEEE Trans. Pattern Anal. Mach. Intell. 34 (2012) 2274–2282, https://doi.org/10.1109/TPAMI.2012.120.

[31] D. Stutz, Superpixel segmentation: an evaluation, in: J. Gall, P. Gehler, B. Leibe (Eds.), Ger. Conf. Pattern Recognit., Springer International Publishing, Cham, 2015, pp. 555–562.

[32] I.T. Jolliffe, Principal Component Analysis, Springer-Verlag,, New York, 2002, https://doi.org/10.1007/b98835.

[33] I.T. Jolliffe, J. Cadima, Principal component analysis: a review and recent developments, Philos. Trans. R. Soc. A Math. Phys. Eng. Sci. 374 (2016), 20150202.

[34] A. Menafoglio, M. Grasso, P. Secchi, B.M. Colosimo, Profile monitoring of probability density functions via simplicial functional PCA with application to image data, Technometrics 60 (2018) 497–510, https://doi.org/10.1080/00401706.2018.1437473.

[35] F. Crete, T. Dolmiere, P. Ladret, M. Nicolas, The blur effect: perception and estimation with a new no-reference perceptual blur metric, in: Hum. Vis. Electron. Imaging XII, 2007. https://doi.org/10.1117/12.702790.

[36] A.M. Khorasani, I. Gibson, A.R. Ghaderi, Rheological characterization of process parameters influence on surface quality of Ti-6Al-4V parts manufactured by selective laser melting, Int. J. Adv. Manuf. Technol. 97 (2018) 3761–3775, https://doi.org/10.1007/s00170-018-2168-6.
[37] Z. Zhu, S. Lou, C. Majewski, Characterisation and correlation of areal surface texture with processing parameters and porosity of high speed sintered parts, Addit. Manuf. 36 (2020), 101402, https://doi.org/10.1016/j.addma.2020.101402.
[38] S. Pomberger, M. Stoschka, M. Leitner, Cast surface texture characterisation via areal roughness, Precis. Eng. 60 (2019) 465–481, https://doi.org/10.1016/j.precisioneng.2019.09.007.
[39] U. Scipioni Bertoli, A.J. Wolfer, M.J. Matthews, J.-P.R. Delplanque, J. M. Schoenung, On the limitations of volumetric energy density as a design parameter for selective laser melting, Mater. Des. 113 (2017) 331–340, https://doi.org/10.1016/j.matdes.2016.10.037.
[40] K.G. Prashanth, S. Scudino, T. Maity, J. Das, J. Eckert, Is the energy density a reliable parameter for materials synthesis by selective laser melting? Mater. Res. Lett. 5 (2017) 386–390, https://doi.org/10.1080/21663831.2017.1299808.
[41] H. Ali, H. Ghadbeigi, K. Mumtaz, Effect of scanning strategies on residual stress and mechanical properties of selective laser melted Ti6Al4V, Mater. Sci. Eng. A 712 (2018) 175–187, https://doi.org/10.1016/j.msea.2017.11.103.
[42] G. Mohr, S.J. Altenburg, K. Hilgenberg, Effects of inter layer time and build height on resulting properties of 316L stainless steel processed by laser powder bed fusion, Addit. Manuf. 32 (2020), 101080, https://doi.org/10.1016/j.addma.2020.101080.